Hydrodynamics of cell-cell mechanical signaling in the initial stages of aggregation

Roland Bouffanais[*] and Dick K. P. Yue

Department of Mechanical Engineering, Massachusetts Institute of Technology, Cambridge, Massachusetts 02139, USA
(Received 15 June 2009; revised manuscript received 17 March 2010; published 28 April 2010)

Mechanotactic cell motility has recently been shown to be a key player in the initial aggregation of crawling cells such as leukocytes and amoebae. The effects of mechanotactic signaling in the early aggregation of amoeboid cells are here investigated using a general mathematical model based on known biological evidence. We elucidate the hydrodynamic fundamentals of the direct guiding of a cell through mechanotaxis in the case where one cell transmits a mechanotactic signal through the fluid flow by changing its shape. It is found that any mechanosensing cells placed in the stimulus field of mechanical stress are able to determine the signal transmission direction with a certain angular dispersion which does not preclude the aggregation from happening. The ubiquitous presence of noise is accounted for by the model. Finally, the mesoscopic pattern of aggregation is obtained which constitutes the bridge between, on one hand, the microscopic world where the changes in the cell shape occur and, on the other hand, the cooperative behavior of the cells at the mesoscopic scale.

I. INTRODUCTION

Life's order is characterized by a cascade of emergent phenomena. This fact was acknowledged long ago by the physicist and Nobel laureate, Erwin Schrödinger, in his distinguished monograph "What is Life" [1]. In this book, the author stresses the challenges faced by the physicist and the chemist in apprehending some of the complexities encountered in life sciences. For instance, self-organization in biological systems pervades nature and takes a central part into the morphogenesis of the vast majority of multicellular living organisms. This is acknowledged by Macklem [2] as one of the two secrets in life based on Schrödinger's treatise [1].

Emergence is better defined as the spontaneous self-organization of a system made of interacting internal agents without intervention by external directing influences [3]. To produce order on a large scale, i.e., a pattern, the system's components—e.g., cells, amoebae—must intercommunicate, interact, and cooperate; these communications and interactions being *local*. Hence, deciphering emergence in a complex biological system requires a clear understanding of the intercommunications and interactions involved in it [2].

The full range of living organisms manifests a direct connection between behavior and internal information processing. In addition to genetic information, all organisms obtain information externally, in the form of signals or stimuli, through their senses. This point was emphasized by Dusenbery [4]. There are three basic mechanisms by which stimuli or signals are transmitted: propagation, diffusion, and flow [4]. For instance, cell motility is critical for many biological processes of spontaneous self-organization. It represents a specific behavior of a microorganism, which is induced by processed information obtained from sensed stimuli or signals available in the surroundings of the cell.

The molecular mechanisms underlying the migration of highly motile cells, also known as amoeboid cell due to the

similarities with the prototypical locomotion of amoebae, have been extensively studied in the past decades [5]. Cell migration is a physically integrated molecular process involving biochemical cascaded intercorrelated with external chemical and mechanical stimuli [6]. From the medical standpoint, stimuli-controlled cell motion plays a key role in the immune system and metastasis responses and spreading [7,8]. From a developmental biology standpoint, the directional rearrangement of cells induced by fields of external stimuli is a key mechanism involved in metazoan morphogenesis; more specifically in early embryonic development: gastrulation followed by organogenesis [9–12].

The influence on morphogenesis of oriented motion up a chemical gradient, i.e., chemotaxis, has been the focus of attention for many years [4,13]. However, the impact of mechanosensing on cell migration, i.e., mechanotaxis, has been relatively overlooked [13], though its importance has proved to be central in recent experiments involving motile amoebae [14–16]. More importantly, from the medical standpoint, mechanotaxis is responsible for regulating leukocyte functions, e.g., increasing motility and phagocytic capabilities [17]. Further to both of these fundamental and medical considerations, it is worth highlighting that mechanotaxis has recently been considered as a way to control and manipulate cell motility [18], which could potentially lead to innovative applications in biotechnology and more precisely in the field of tissue engineering [19].

To investigate the hydrodynamics of mechanotaxis and its effects on the directed motion of cells, a good strategy is to examine and model a simple system made of prototypical motile cells. Many features of amoeboid motility appear to be universal across species and cell types [20], hence reinforcing the importance of an hydrodynamic-based model for mechanotaxis. The social amoebae *Dictyostelium discoideum* (Dd) has been a microorganism of choice for studying a variety of basic processes in morphogenesis, including cell-cell chemical signaling, signal transduction, and cell motility. Indeed, this simple eukaryote is a genetically, biochemically, and cell-biologically tractable model organism [5,8,21,22] with an extensively studied social life [22,23]. The many

*bouffana@mit.edu

reasons for developing a model based on Dd have recently been discussed in detail in [24]. This amoeba lacks a cell wall and moves by crawling. Such amoeboid motility is induced by complex internal processes responsible for the changes in the cell shape over time (see [25] for an introduction and [26] for a recent review on this topic). Dd is also a prototypical motile cell of interest as it exhibits a remarkable interplay between single-cellular and multicellular behaviors. In the presence of nutrients, individual Dd cells move, feed, and divide every few hours. Food scarcity leads to a behavioral change in Dd toward a collective aggregation. Although the change of behavior has a chemical origin, there is now accumulating evidence that mechanotaxis plays a key role in the early aggregation stages [14–16]. The cells integrate the mechanical stress through mechanotransduction at their surface into an intracellular biochemical signal acting on the control system, which triggers a cellular response resulting in a change of orientation [13–15].

As already mentioned earlier, deciphering a complex self-organization behavior in a biological system such as aggregating amoebae requires a clear understanding of the intercommunications and interactions involved in it. Since the seminal work of Turing on chemotaxis [27], there is now an enormous body of knowledge on that specific chemical signaling between cells. We know from recent experiments [14–16] that mechanotaxis is another overarching component of these local interactions responsible for initiating the aggregation of amoebae. It seems therefore timely to perform an investigation of mechanotaxis from a theoretical standpoint, which is the central objective of the present work. Our focus is on analytical analyses and results, but our aim is to emphasize physical intuition and connections to the real-life biological systems.

The outline of the present paper is as follows. Section II presents a modeling approach of the problem in which the governing equations and associated boundary conditions are derived. A general representation of the cell boundary motion is discussed in Sec. III, followed by the determination of the associated mechanotactic stimulus field in Sec IV. Section V presents the mechanosensing capabilities of the stimulus field and in Sec. VI the results of a model for the stimuli-controlled movement of the amoeboid cells are analyzed. Finally, conclusions are drawn in Sec. VII.

II. MODELING APPROACH AND PROBLEM FORMULATION

A. General considerations

To gain insight into local mechanotactic cell-cell signaling, we propose a simplified model epitomizing the communication through hydrodynamic interaction between cells when aggregation is initiated. In the early aggregation stages, cells which are of typical size $\ell = 10$ μm are widely separated. Therefore, it is not of primary importance to consider this many-body problem as a whole. Instead, we focus our attention on an "isolated" subsystem of the multicellular aggregating structure. This hypothesis of isolation remains valid as long as the distance between the internal cells of the subsystem, i.e., the characteristic size of the subsystem, is
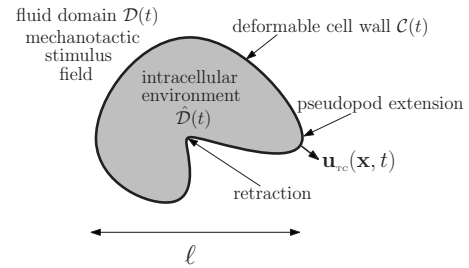

FIG. 1. Schematic of a transmitting cell with pseudopod extensions and retractions generating a mechanotactic stimulus field in the extracellular fluid domain.

smaller than the distances to the other neighboring cells. The most elementary subsystem comprises two cells mechanically interacting through the fluid flow. To simplify further the analysis, we assume that these two interacting cells have noninterchangeable roles: one cell, the transmitting cell (TC), is responsible for generating the hydrodynamic signal while the other cell, the receiving cell (RC), experiences the mechanotactic stimulus field generated by the TC on its surface wall. The central goal of this study is to show that through integrated mechanosensing of the stress at its surface, the RC can be directly guided [4] toward the TC, typical of an aggregative response.

Before dealing with the mechanosensing at the RC's surface, it is instrumental to obtain first the mechanotactic stimulus field generated by the TC in its motile behavior, which is at small scale and hence at very low Reynolds number. The specificities of the biophysical and mechanical principles of locomotion at low Reynolds number, though counterintuitive from the human-scale viewpoint, are well known [28,29]. Microbes evolve in a quasi-inertia-free environment where the viscosity is of paramount importance. Swimming strategies employed by large organisms that operate at large Reynolds numbers, such as fish, are ineffective at the micron scale [29]. Hence, microorganisms and cells essentially experience viscous drag which has to be employed in a nonreversible manner to yield a net motion [28,30]. This is the Stokesian realm described by Purcell [28] as "very slow, majestic, and regular."

The amoeboid crawling is one of the many ways of locomotion at the micron scale and is essentially two dimensional (2D) [25,26,31]. The shape evolution is the result of controlled internal cytoplasmic mechanisms, whose details are not relevant to the present study. During locomotion, cells constantly change shape by rapidly protruding and retracting extensions known as pseudopods [25]. Here we focus on the hydrodynamics of the extracellular environment subject to a prescribed evolution of the intracellular matrix, leading to a known kinematic of the TC's surface boundary.

B. Governing equations and boundary conditions

We formulate here the problem of the mechanotactic stimulus field, introducing the key notations and the governing equations. For definiteness, consider one TC generating a mechanical stimulus field (see the schematic representation in Fig. 1). The signal information is carried by mechanical

stress associated with the viscous flow generated by changes of the TC shape reminiscent of amoeboid surface crawling [25]. Our focus is on the hydrodynamics of the extracellular environment denoted as $\mathcal{D}$ (see Fig. 1).

We consider a cell placed in an otherwise quiescent fluid of viscosity μ. Given the small scales ($\ell = 10 \ \mu$m) and hence the low Reynolds number, the time evolution of the TC wall, $\mathcal{C}(t)$, yields an incompressible Stokes flow that is instantly acting on any RC present in its vicinity. The velocity field **u** and pressure field p are solutions of the Stokes equations [32]

$$\mu \Delta \mathbf{u} = \nabla p, \tag{1}$$

$$\nabla \cdot \mathbf{u} = 0, \tag{2}$$

plus appropriate boundary conditions given by the no-slip boundary condition for the velocity field **u** on amoeba's moving surface $\mathcal{C}(t)$ and the vanishing of **u** far away

$$\mathbf{u}(\mathbf{x},t) = \mathbf{u}_{\text{TC}}(\mathbf{x},t), \quad \mathbf{x} \text{ on } \mathcal{C}(t), \tag{3}$$

$$\mathbf{u}(\mathbf{x},t) = 0, \quad \mathbf{x} \to \infty, \tag{4}$$

where $\mathbf{u}_{\text{TC}}$ is the time-dependent velocity of the cell boundary. The subscript "TC" stands for transmitting cell to emphasize the fact that the cell wall motion is the actual source of mechanotactic signal. Note that the Stokes equations (1) and (2) are linear and independent of time, a fact with important consequences for the flow physics.

The time dependence of the present problem comes from the no-slip condition (3) at the moving surface. The linear and time independence of the governing equations for motility at small scales lead to two important properties [28,29]: the rate independence and the so-called scallop theorem. The rate independence property relates to the fact that the distance traveled by any microorganism does not depend on the rate of change of the surface $\mathcal{C}(t)$ but only on the sequence of geometric configurations taken by the $\mathcal{C}(t)$ over time. The scallop theorem states that if the periodic sequence of shapes displayed by a microswimmer is identical under a time-reversal transformation, then the microswimmer cannot have net motion. In the present case, the net motion of the cell hence results from nonreciprocal changes of its shape. The counterintuitive nature of the locomotion at low Reynolds number is also apparent when one realizes the difficulty of simply predicting the direction of motion [28,33].

III. GENERAL REPRESENTATION OF THE CELL BOUNDARY MOTION

A. General considerations

The change in the shape of the transmitting cell wall is the source of the fluid flow and consequently of the mechanotactic stimulus field, as pointed out in Sec. II after Eq. (3). Therefore, it is critical to obtain an appropriate representation for the shape. In a 2D framework, one powerful yet compact method is to conformally map the domain $\mathcal{D}(t)$ exterior to the cell boundary represented by the Jordan curve $\mathcal{C}(t)$ (in z space, see Fig. 1) onto the exterior of the unit disk
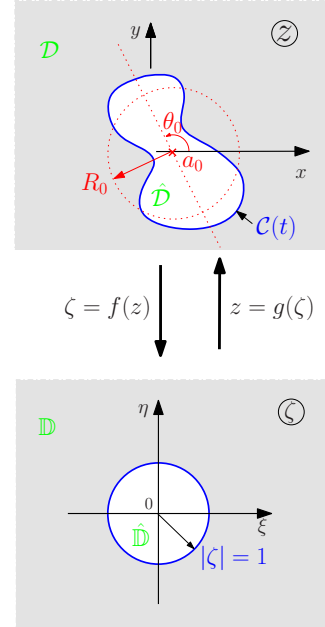

FIG. 2. (Color online) Schematic representation of direct and inverse mappings and the internal and external domains. The set (a_0, R_0, θ_0) comprises the three conformal elements associated with the fluid domain $\mathcal{D}$.

$\mathbb{D}$ (in ζ space). For clarity, the notations associated with the mapping, domains, and spaces are schematically shown in Fig. 2. From the physical standpoint, the moving-boundary domain $\mathcal{D}$ in the z space is the fluid domain subject to a Stokes flow and corresponds to the infinite domain outside $\mathbb{D}$; the complement $\hat{\mathcal{D}}$ of the fluid domain $\mathcal{D}$, i.e., the interior of $\mathcal{D}$, is the intracellular environment and corresponds to the interior of the unit disk logically denoted as $\hat{\mathbb{D}}$.

B. Conformal elements

The Riemann mapping $\zeta = f(z)$ is unique and should be such that it exhibits a simple pole at infinity [34]. In the present study, the inverse exterior mapping $z = f^{-1}(\zeta) = g(\zeta)$, from the exterior unit disk $\mathbb{D}$ onto the fluid domain $\mathcal{D}$ is of main interest and shall only be considered in the sequel. This inverse mapping is conformal and the mapping function g admits a simple Laurent expansion which can be expressed generally as

$$g(\zeta) = a_1(t)\zeta + a_0(t) + \frac{a_{-1}(t)}{\zeta} + \frac{a_{-2}(t)}{\zeta^2} + \cdots, \quad \zeta \in \mathbb{D},$$

$$\tag{5}$$

where the time dependency of the complex coefficients of the series is directly connected to the sole time-dependent equation of the problem, namely, the no-slip boundary condition (3) enforced on the moving cell boundary $\mathcal{C}(t)$. It is convenient to express the first complex coefficient in its polar form, i.e., $a_1(t) = R_0(t)e^{i\theta_0(t)}$, which uniquely defines the (outer) conformal radius R_0 and the conformal orientation θ_0 [35]. The second coefficient, a_0, of the Laurent series (5)

represents the conformal center which also has a unique definition [36].

It is important to note that the (external) conformal mapping theory provides a convenient, yet not straightforward, way of defining a unique center, radius, and orientation, which can be interpreted as the fundamental characteristics of the cell shape. Note also that, in general, the conformal center a_0 is different from the centroid of the interior domain $\hat{\mathcal{D}}$, although the difference is often small. There are several other approaches to this same measure of the "spread" of $\mathcal{D}$. For instance, the outer conformal radius is identical to the transfinite diameter (see [37]). Other approaches involve polynomial approximation (Chebyshev's constant) or potential theory (logarithmic capacity, Robin's constant) (see [38] for more details). The outer conformal radius, like the transfinite diameter, the logarithmic capacity, and the Robin's constant are all conformal invariants [37].

C. Shape normalization and representation

If one considers various domains having the same shape, but shifted, dilated, and rotated, it is possible to find a unique normalized inverse exterior mapping characterizing the shape only and defined as its fingerprint [39]. The normalization procedure consists of three basic steps in the complex plane: a translation of amplitude $-a_0$, followed by a dilation by a factor $1/R_0$, and finally a rotation about the origin by an angle $-\theta_0$. Mathematically, the normalization leads to the definition of the shape fingerprint [39] as a univalent inverse exterior mapping, denoted by h, defined on $\mathbb{D}$, given by

$$z = a_0(t) + R_0(t)e^{i\theta_0(t)}h(\zeta), \quad \zeta \in \mathbb{D}, \qquad (6)$$

and admitting the Laurent series

$$h(\zeta) = \zeta + \frac{\eta_1(t)}{\zeta} + \frac{\eta_2(t)}{\zeta^2} + \cdots, \quad \zeta \in \mathbb{D}, \qquad (7)$$

where $\eta_k(t) = a_{-k}(t)/a_1(t)$, $k \geq 1$.

The normalization procedure (6) gives access to the set of conformal elements (a_0, R_0, θ_0) (shown in red dashed lines in Fig. 2) and the fingerprint h, providing a unique and complete characterization of any 2D located shape. Note that this procedure is completely general and can be applied to any cell shape, even those extremely stretched and with multiple pseudopod extensions and retractions [22,40]. Each term in $1/\zeta^k$ in Eq. (7) has a clear geometric meaning associated with a polygonal perturbation of the unit circle; more precisely to a $(k+1)$-gonal type perturbation, also referred to as non-self-intersecting hypotrochoids of order k [41]. For example, the leading terms in $1/\zeta$ and $1/\zeta^2$ correspond, respectively, to a digonal and an equilateral-triangle-type of perturbation.

The essential difference between the conformal elements and the shape fingerprint is that the former is independent of the relative distance to the cell δ in the stimulus field, which is directly related to the shape fingerprint through
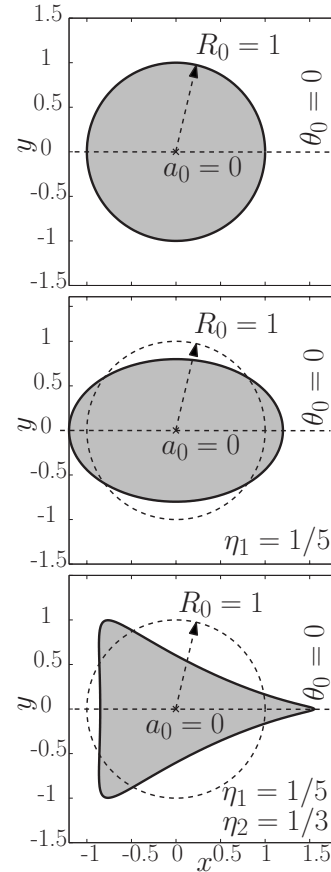

FIG. 3. From the unit circle (top), to an ellipse with $\eta_1 = 1/5$ (middle), to the final shape with $\eta_1 = 1/5$ and $\eta_2 = 1/3$ (bottom).

$$\delta = \frac{|z - a_0(t)|}{R_0(t)} = |h(\zeta)|. \qquad (8)$$

For a given δ, the number of useful terms in the asymptotic series (7) is limited by the presence of noise and by the limited mechanosensing capabilities on the surface of the receiving cells. Without loss of generality, we consider only the first two perturbation terms leading to a mapping and associated fingerprint function expressed, respectively, as

$$g(\zeta) = a_1\zeta + a_0 + \frac{a_{-1}}{\zeta} + \frac{a_{-2}}{\zeta^2}, \qquad (9)$$

$$h(\zeta) = \zeta + \frac{\eta_1}{\zeta} + \frac{\eta_2}{\zeta^2}. \qquad (10)$$

The associated geometric shape construction process is highlighted in Fig. 3 for a (conformally normalized) shape taken to represent an idealized TC. This idealized cell presents three pseudopod extensions (two smaller identical ones in the directions $\theta = 2\pi/3$ and $\theta = 4\pi/3$ and a more extended one in the direction $\theta = 0$) and limited retractions.

IV. MECHANOTACTIC STIMULUS FIELD

A. Driving boundary condition

The general conformal representation of the cell shape presented in Sec. III, mainly through Eqs. (5)–(7), allows us to parametrize its time evolution, e.g., to account for pseudo-pod extensions or retractions, by specifying the time variations of $(a_0, R_0, \theta_0, \{\eta_k\}_{k \geq 1})$. The driving velocity on the surface of the TC reads

$$U_{TC} = u_{TC} + i v_{TC} = \frac{\partial z}{\partial t} = \dot{a}_1 \sigma + \dot{a}_0 + \frac{\dot{a}_{-1}}{\sigma} + \frac{\dot{a}_{-2}}{\sigma^2}, \quad (11)$$

where $\sigma = e^{i\theta}$ is the running variable on the conformal image of the cell boundary $\mathcal{C}(t)$.

B. General solution for the Stokes flow

For 2D Stokes flow, the streamfunction ψ and pressure field are, respectively, solutions of homogeneous biharmonic and harmonic equations [32]. With the problem cast in terms of analytic functions, conformal mapping is a straightforward and powerful technique to devise explicit solutions to this intricate moving-boundary problem. Unlike harmonic equations, the biharmonic equation is however not preserved under conformal mapping [42]. Despite this fact, general conformal-mapping-based solutions of the biharmonic equation in 2D have been available in elasticity theory [41] and for Stokes flow [30,31,42].

Any 2D Stokes flow solution of Eqs. (1) and (2) can be expressed as

$$u + iv = \phi(z) - z \overline{\phi'(z)} + \overline{\chi(z)}, \quad (12)$$

$$p = -4\mu \, \mathrm{Re}[\phi'(z)], \quad (13)$$

where complex potentials $\phi(z)$ and $\chi(z)$ are holomorphic functions in $\mathcal{D}(t)$ [30,31,41,42]. From Eqs. (12) and (13), one can obtain directly the stress tensor $\boldsymbol{\sigma}$ carrying the mechanotactic signal.

Both ϕ and χ depend on $\mathbf{u}_{TC}$ which has a known expression (11) in the ζ plane. Hence, these functions shall be obtained analytically through conformal mapping [30,31,41], which allows Eq. (12) to be cast as

$$u^* + iv^* = \phi^*(\zeta) - \frac{g(\zeta)}{\overline{g'(\zeta)}} \overline{\phi^{*'}(\zeta)} + \overline{\chi^*(z)}, \quad (14)$$

where ( )* denotes the expression of a function in the ζ plane, with the mapping $\zeta = f(z)$ and its inverse $z = g(\zeta)$. This expression of the complex fluid velocity in the ζ plane allows one to explicitly connect the complex potentials with the time-varying geometric parameters characterizing the cell shape evolution, through the driving no-slip condition now expressed in the ζ plane

$$\dot{a}_1 \sigma + \dot{a}_0 + \frac{\dot{a}_{-1}}{\sigma} + \frac{\dot{a}_{-2}}{\sigma^2} = \phi^*(\sigma) - \frac{g(\sigma)}{\overline{g'(\sigma)}} \overline{\phi^{*'}(\sigma)} + \overline{\chi^*(\sigma)}, \quad (15)$$

and more specifically on the TC image boundary $|\sigma| = 1$ or $\sigma = e^{i\theta}$. Using the holomorphic character of the complex po-

tentials and the mapping function in $\mathbb{D}$ (including at the point at infinity), one may recast the boundary formulation (15) into a functional equation for ϕ^* that is equivalent to ordinary Fredholm equations of the second kind using Cauchy's formula for infinite region [41]. Although this technical step is far from being trivial from a purely mathematical standpoint, it is nonetheless instrumental as it gives a general way of calculating the complex potential for any inverse exterior mapping represented by a Laurent series such as Eq. (5). The use of Cauchy's formula for infinite regions is suggested by the fact that one aims at obtaining an expression of $\phi^*(\zeta)$ for $\zeta \in \mathbb{D}$ based on some boundary information of $\phi^*(\sigma)$ for $\sigma \in \partial\mathbb{D}$. One can readily prove the following general expressions:

$$\phi^*(\zeta) = -\frac{1}{2\pi i} \oint_{\partial\mathbb{D}} \frac{U^*_{TC}(\sigma)}{\sigma - \zeta} d\sigma, \quad (16)$$

which, given the no-slip driving boundary condition (11), leads to

$$\phi^*(\zeta) = \frac{\dot{a}_{-1}}{\zeta} + \frac{\dot{a}_{-2}}{\zeta^2}. \quad (17)$$

In order to determine the expression of χ, it is convenient to recast Eq. (15) as

$$\chi^*(\sigma) = \overline{\dot{a}}_0 + \frac{\overline{\dot{a}}_1}{\sigma} + \frac{\overline{g(\sigma)}}{\overline{g'(\sigma)}} \phi^{*'}(\sigma). \quad (18)$$

Using the expression (17) for ϕ^*, the fact that on $\partial\mathbb{D}$ $\overline{g(\sigma)} = \overline{g}(1/\sigma)$, and Cauchy's formula for the infinite region, one finally obtains

$$\chi^*(\zeta) = \overline{\dot{a}}_0 + \frac{\overline{\dot{a}}_1}{\zeta} - \frac{\overline{g}(1/\zeta)}{g'(\zeta)} \left[\frac{\dot{a}_{-1}}{\zeta^2} + \frac{2\dot{a}_{-2}}{\zeta^3} \right] \quad (19)$$

or more explicitly

$$\chi^*(\zeta) = \overline{\dot{a}}_0 + \frac{\overline{\dot{a}}_1}{\zeta} - \frac{\dfrac{\overline{a_1}}{\zeta} + \overline{a_0} + \overline{a_{-1}}\zeta + \overline{a_{-2}}\zeta^2}{a_1 - \dfrac{a_{-1}}{\zeta^2} - \dfrac{2a_{-2}}{\zeta^3}} \left[\frac{\dot{a}_{-1}}{\zeta^2} + \frac{2\dot{a}_{-2}}{\zeta^3} \right]. \quad (20)$$

With the expression of $\phi^*(\zeta)$ and $\chi^*(\zeta)$ given, respectively, by Eqs. (17) and (20), we have finally access to the exact solution of the problem in the ζ plane, in terms of the complex coefficients $(a_1, a_0, a_{-1}, a_{-2})$, also equivalent to $(a_0, R_0, \theta_0, \eta_1, \eta_2)$, characterizing the geometric evolution of the cell boundary $\mathcal{C}(t)$. The expression of the velocity and pressure solutions of the Stokes equations (1) and (2) in the extracellular environment $\mathcal{D}$ of the z plane is trivially obtained if the direct mapping $\zeta = f(z)$ is known.

From the general solution Eqs. (17) and (20), it is seen that in the absence of changes in the cell boundary, i.e., $\dot{a}_1 = \dot{a}_0 = \dot{a}_{-1} = \dot{a}_{-2} = 0$, ϕ^* and χ^* are identically zero and there is no flow, as expected. If one considers a bubble growing or collapsing while maintaining a circular shape, one readily retrieve

$$\phi^*(\zeta) = 0, \quad (21a)$$

$$\chi^*(\zeta) = \frac{\dot{R}_0(t)}{\zeta} \tag{21b}$$

from the general solution of the 2D Stokes flow. For this specific problem, the conformal radius R_0 is the sole time-dependent problem as $\theta_0 = 0$ (no conformal orientation for a circular shape), a_0 is constant, and $\eta_1 = \eta_2 = 0$. From the complex potentials (21a) and (21b), one can deduce the expression of the velocity in polar coordinates in the complex z plane

$$u + iv = \frac{\dot{R}_0 R_0}{r} e^{-i\theta}. \tag{22}$$

This result is a particular case of general time-evolving bubbles in a 2D Stokes flow studies by Tanveer and Vasconcelos [43].

The fluid is quiescent at infinity provided that both complex potentials vanish there. Since the point at infinity in the ζ plane maps to the point at infinity in the z plane, the conditions $\phi(\infty) = 0$ and $\phi^*(\infty) = 0$ are equivalent and is valid irrespectively of the shape and its changes given the expression (17) for ϕ^*. The same applies to $\chi(\infty)$ and $\chi^*(\infty)$. However, having a vanishing χ^* at infinity imposes a constraint on the complex coefficients of the conformal mapping and their time derivatives

$$a_1(t)\overline{\dot{a}_0(t)} = \overline{a_{-2}(t)}\dot{a}_{-1}(t), \tag{23}$$

as a consequence of Eq. (20). This is a constraint on the cell wall and its temporal evolution, which is clearer when expressed as

$$\dot{a}_0 = \eta_2(t)[\dot{R}_0\overline{\eta_1(t)} - iR_0(t)\dot{\theta}_0\overline{\eta_1(t)} + R_0(t)\overline{\dot{\eta}_1}]e^{i\theta_0(t)}. \tag{24}$$

Given the definition of the conformal elements and the shape representation introduced, respectively, in Secs. III B and III C, a physical interpretation of the constraint (24) is possible. The time derivative, $\dot{a}_0$, of the conformal center represents the translational velocity of the cell in its motion, while $\dot{\theta}_0$ is associated with the angular velocity of the cell (presuming that somehow the cell is able to spin). The time evolution of the conformal radius, measured by $\dot{R}_0$, can be interpreted as the growing or collapsing rate of the cell depending on the sign of $\dot{R}_0$. Both the digonal and triangular coefficients, η_1 and η_2, appear in Eq. (24), while only the time derivative $\dot{\eta}_1$, rate of elliptical extension or retraction, is involved. From Eq. (24), it is clear that the cell's translation velocity $\dot{a}_0$ is directly proportional to the amplitude of the triangular coefficient η_2. Moreover, three factors contribute independently to that amoeboid motile translational motion: the growing or collapsing rate $\dot{R}_0$, the angular velocity $\dot{\theta}_0$, and the rate of elliptical extension or contraction $\dot{\eta}_1$. The natures of these factors are different: the first two relate to the shape normalization, while the former is purely geometrical and associated with the shape fingerprint definition.

C. Idealization of the cell boundary evolution

In this study, our primary focus is on mechanotactic cell-cell signaling and not on cell motility *per se*. Even though cell motility is generally a source of mechanotactic signal, it is possible for a cell to produce a mechanotactic stimulus field while remaining stationary. From the discussion associated with Eq. (24), it is clear that a TC with vanishing $\dot{R}_0$, $\dot{\theta}_0$, and $\dot{\eta}_1$ does not move, but clearly the mechanotactic signal can still be nonzero [cf. Eqs. (17) and (20)].

Without loss of generality, let us consider a hypothetical deformation of the cell in which the conformal radius R_0 and the conformal orientation θ_0 are kept fixed, which corresponds to having a_1 constant. This assumption is readily justified by the real-life observations of cell behaviors. It is equivalent to assume the characteristic size of the cell to be constant over time, which is practically the case given the constant cytoplasmic internal volume of the cell. On the other hand, considering the conformal orientation as constant is similar to neglecting global solid-state-like rotation of the cell, which is legitimate as the typical motion of a cell involved in amoeboid crawling is primarily translational [22,25].

For simplicity and without loss of generality, we further impose that the complex coefficient η_1 remains constant over time. This leads to having the TC remaining stationary and to an additional simplification of the problem achieved by having only η_2 to be time dependent. Indeed, this is sufficient to yield pseudopod extensions or retractions and to generate a mechanotactic stimulus field equivalent to one encountered in real-life aggregating systems. At this point, it is worth emphasizing that for the TC to be able to generate a mechanotactic signal while not moving is of significant importance as we shall see in Sec. V.

The triangular coefficient η_2 is taken to have pulsatile time variations of period $T = 2\pi/\omega$, characteristics of the cyclic nature of the mechanics of cellular motility [44]. Figure 4 presents these variations of the shape of the TC over a period for given amplitudes of η_1 and η_2. For this idealized cell boundary evolution, the general results of Sec. IV B can be recast in a simplified set of equations. The driving velocity of the TC is obtained from Eq. (11) with $\dot{a}_{-2} = a_1\dot{\eta}_2$,

$$U_{\text{TC}}^*(\sigma) = \frac{a_1\dot{\eta}_2}{\sigma^2}, \tag{25}$$

while the complex potentials in the ζ space read

$$\phi^*(\zeta) = \frac{R_0 e^{i\theta_0}\dot{\eta}_2}{\zeta^2}, \tag{26a}$$

$$\chi^*(\zeta) = 2R_0 e^{i\theta_0}\dot{\eta}_2 \left[\frac{1/\zeta + \overline{\eta_1}\zeta + \overline{\eta_2}\zeta^2}{2\eta_2 + \eta_1\zeta - \zeta^3} \right]. \tag{26b}$$

Without loss of generality, the TC, being designed not to move, is considered to be conformally centered, i.e., $a_0 = 0$.

It is worth stressing that the idealization of the TC boundary evolution in this section, while simplifying somewhat the theoretical analysis, is primarily designed to account for known biological factors focusing on the generation of
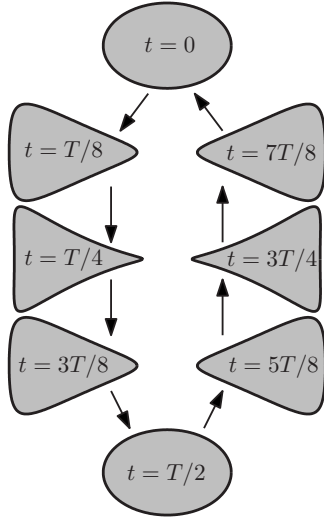
FIG. 4. Time evolution of the shape of the transmitting cell over a period T. The constant digonal coefficient is $\eta_1 = 1/5$ and the amplitude of the pulsatile triangular coefficient is taken as $\eta_2 = 1/3$.

pseudopod extensions as source of a mechanotactic stimulus field. This is further studied in the next section.

V. MECHANOSENSING CAPABILITIES OF THE STIMULUS FIELD

A. General considerations

The pulsatile variations of the shape of TC create a mechanotactic stimulus field represented by Eq. (26) in the ζ plane. The key issue here is to know whether a RC can be directly guided by this stimulus field, i.e., whether it can obtain information about the orientation of the stimulus field with respect to itself.

The term "guiding," be it direct or indirect, is due to Dusenbery who gave a comprehensive discussion (the entire chapter 17) about this topic in his monograph "Sensory Ecology" [4]. Briefly, the term guiding denotes a behavioral response of an organism detecting a stimulus that can be used to move closer to a specific goal. In the present framework, we study the possible response of the RC placed in the stimulus field of mechanical origin generated by the TC. In itself, the TC constitutes the ultimate goal for the RC in its approach phase. The guiding is said to be direct when the sensing organism follows a relatively straight-line path to the goal. The chemotactic-based aggregation of Dd is one example of direct guiding. In contrast, indirect guiding is typical of biased random walks employed by bacteria such as *E. coli* [45]. The distinction is important because the direct approach requires that the sensing organism has some mechanism for rapidly determining the direction to the goal [4]. Note that we exclude here passive changes in the direction of locomotion, such as cell reorientation, due to hydrodynamic interactions, which is not based on a stimulus-response mechanism.

In order for an organism to determine the orientation toward its goal when placed in a stimulus field, it is necessary
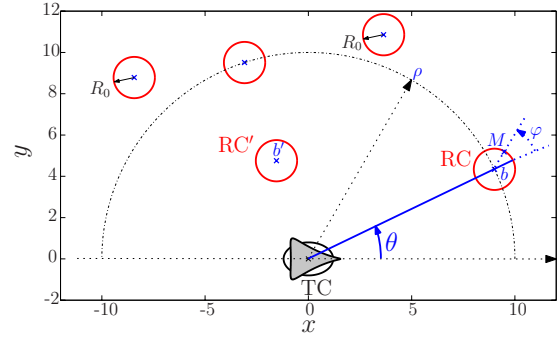

FIG. 5. (Color online) TC and different superimposed positions of RCs centered at $b = a_0 + \rho e^{i\theta}$ in the physical z space. The local angle φ serves to parameterize the position of mechanotransducers at the cell's surface.

to measure the spatial variation of the stimulus intensity. Amoebae Dd cells have mechanoreceptors distributed along their cell walls [14,15], allowing them to perform an integrated simultaneous sampling of the mechanical stress at their surface, given the rapid signal mechanotransduction [46]. The exact distribution of these sensors is still not clearly known, although there is evidence that the protruding front, also known as "head" of the cell wall, is more mechanosensitive than the retracting "tail" [14,15]. For simplicity, we assume that mechanotransducers are continuously distributed along the RC's cell wall, measuring the root mean square (rms) of the local surface stress. Details about the mechanisms of cell responses to mechanical stimuli can be found in the review by Janmey and McCulloch [13]. Although there is a specific report of mechanosensitivity to shear stress [16], most of the studies commonly consider that cells are mechanosensitive to the traction generated by the local stress field, which includes both normal pressure and shear stresses [13–15].

To assess the capabilities of RCs in detecting the signal originated from the TC with varying distance and bearing, we consider different positions of the RC, centered at $b = a_0 + \rho e^{i\theta}$, at a distance ρ and a bearing θ (measured from the conformal axis of the TC) to the TC, as depicted schematically in Fig. 5. We further assume for simplicity that the RC has an idealized circular shape of radius equal to the conformal radius of the TC, namely, R_0. As the mechanosensation at the RC's surface is considered, we also parameterize any point M at the surface by a local angle φ measured from the axis making an angle θ with respect to TC's conformal axis. This local parameterization is chosen for convenience, so that, for any RC placed in the stimulus field, the value $\varphi = \pi$ points toward the goal to reach, i.e., the TC, as shown in Fig. 5.

B. Influence of the presence of the receiving cell on the transmitted signal

When aggregation is initiated, the TC and RC are widely separated. The Stokes flow generated by the TC is locally perturbed by any RC present. In the current framework, where only an isolated subsystem is considered (cf. Sec. II A), only one single RC participate to the local perturbation

of the mechanotactic stimulus field acting on it. Given the large distance between the two cells, the enforcement of the no-slip boundary condition on the RC's surface can be obtained by applying the method of reflection [32,47] and the circle theorem for Stokes flow [48,49], given RC's assumed circular shape.

The shape fingerprint $Z=h(\zeta)=(z-a_0)/(R_0e^{i\theta_0})$ represents a natural variable in this problem considered from the physical space standpoint. It can be seen as the general conformally normalized variable based on the discussion in Sec. III B. Owing to the biological factors that led to the idealization of the cell wall evolution presented in Sec. IV C, the set of conformal elements (a_0, R_0, θ_0) is constant in time, while the coefficient η_2 in the Laurent series (10) of $Z = h(\zeta)$ has pulsatile variations and is the source of the stimulus field. As mentioned in Sec. IV B, one seeks the expression of the various hydrodynamic fields of interest in the z space or similarly in the Z space. To this aim, the inversion of the shape fingerprint series h can be performed up to any order; this inversion is guaranteed by the nature of the univalent fingerprint h and the form of its Laurent series appearing in Eq. (10). For instance, up to the sixth order in $1/Z$, the inversion gives

$$\frac{1}{\zeta} = \frac{1}{Z} + \frac{1}{Z^3} + \frac{\eta_2}{Z^4} + \frac{2\eta_1^2}{Z^5} + O\left(\frac{1}{\delta^6}\right), \tag{27}$$

with $\delta=|Z|$. Subsequent higher powers of $1/\zeta$ can be found accordingly. In practice, the assumed large distance between the TC and the RC (i.e., $\rho \gg \ell = R_0$) allows us to considering the leading-order terms in the following hydrodynamic quantities. The general expression of the stress tensor $\boldsymbol{\sigma}$ in terms of the complex derivatives of the two complex potentials ϕ and χ reads

$$\sigma_{xx} = 2\mu \, \text{Re}[2\phi'(z) - \bar{z}\phi''(z) + \chi'(z)], \tag{28a}$$

$$\sigma_{yy} = 2\mu \, \text{Re}[2\phi'(z) + \bar{z}\phi''(z) - \chi'(z)], \tag{28b}$$

$$\sigma_{xy} = 2\mu \, \text{Im}[\bar{z}\phi''(z) - \chi'(z)]. \tag{28c}$$

Given Eqs. (25), (27), and (28), we have access to the unperturbed stimulus field at the leading order

$$\sigma_{xx} = -2\mu\omega\eta_2 \cos(\omega t)\text{Re}\left(\frac{4}{Z^3} + \frac{6\bar{Z}}{Z^4}\right), \tag{29a}$$

$$\sigma_{yy} = -2\mu\omega\eta_2 \cos(\omega t)\text{Re}\left(\frac{4}{Z^3} - \frac{6\bar{Z}}{Z^4}\right), \tag{29b}$$

$$\sigma_{xy} = -2\mu\omega\eta_2 \cos(\omega t)\text{Im}\left(-\frac{6\bar{Z}}{Z^4}\right), \tag{29c}$$

in terms of the conformally normalized variable Z in the physical plane, given $\dot{\eta}_2 = \omega\eta_2 \cos(\omega t)$. As noted earlier, the perturbed complex potentials, denoted $\tilde{\phi}$ and $\tilde{\chi}$, are obtained through a "circular reflection" at the leading order, i.e., by the joint application of the method of reflection and the circle theorem for Stokes flow on the RC's circular boundary. From

the general solution given in [30] for a problem with a circular boundary and the circle theorem for Stokes flow [48,49], one can prove that at the leading order, $O(1/\delta^4)$, the perturbed potentials are

$$\tilde{\phi}(Z) = \phi(Z), \tag{30a}$$

$$\tilde{\chi}(Z) = \chi(Z) - R_0\dot{\eta}_2\left[\frac{1}{\left(\bar{\beta} + \dfrac{1}{Z-\beta}\right)^2} + \frac{2\left(\bar{\beta} + \dfrac{1}{Z-\beta}\right)}{\left(\beta + \dfrac{1}{\bar{Z}-\bar{\beta}}\right)^3}\right], \tag{30b}$$

where $\beta = b/a_1 = b/(R_0e^{i\theta_0})$. Hence, in the neighborhood of the RC, the stimulus field reads

$$\tilde{\sigma}_{xx} = -2\mu\omega\eta_2 \cos(\omega t)\text{Re}\left[\frac{4}{Z^3} + \frac{6\bar{Z}}{Z^4} + \Psi(Z)\right], \tag{31a}$$

$$\tilde{\sigma}_{yy} = -2\mu\omega\eta_2 \cos(\omega t)\text{Re}\left[\frac{4}{Z^3} - \frac{6\bar{Z}}{Z^4} - \Psi(Z)\right], \tag{31b}$$

$$\tilde{\sigma}_{xy} = -2\mu\omega\eta_2 \cos(\omega t)\text{Im}\left[-\frac{6\bar{Z}}{Z^4} - \Psi(Z)\right], \tag{31c}$$

where

$$\Psi(Z) = \frac{2}{(Z-\beta)^2}\left[\left(\frac{1}{\bar{\beta}^3} - \frac{1}{\beta^3}\right) - 3\left(\frac{1}{\bar{\beta}^4(Z-\beta)} - \frac{1}{\beta^4(\bar{Z}-\bar{\beta})}\right)\right] \tag{32}$$

is directly connected to the derivative with respect to Z of $\tilde{\chi} - \chi$, as per Eqs. (27) and (30b) at the prevailing leading order.

When the RC is infinitely remote from the TC, the perturbation of the stimulus field vanishes. Indeed in that case, ρ tends to infinity and $|1/\beta|$ tends to zero. Hence we have $\tilde{\chi} = \chi$ and also $|\Psi(Z)| \to 0$.

With hindsight, it may be noted that Eq. (31) [supplemented with Eq. (32)] is the nonlinear functional governing the more general problem of determining TC's complete set of geometric characteristics based on mechanotransduction at the RC's surface. Intrinsically, this belongs to the broad family of inverse problems which are generally not well-posed problems. A sensitivity analysis reveals the level of uncertainty associated with each unknown geometric parameters depending on the relative distance $\delta=|Z|$ to the TC. Independent local perturbation analyses show that the conformal elements (a_0, R_0, θ_0) have, respectively, their highest correction term varying in $1/\delta^4$, $1/\delta^3$, and $1/\delta^3$. This shows that for a given distance $\delta(\gg 1)$ away, the position (distance and direction) a_0 of the TC can be detected with 1 order higher accuracy than its dimension (R_0) or orientation (θ_0). However, it is critical to understand that the problem of direct guiding, which is at the heart of mechanotactic cell-cell signaling, is far less stringent than the inverse detection problem. This fact is demonstrated in the following sections.
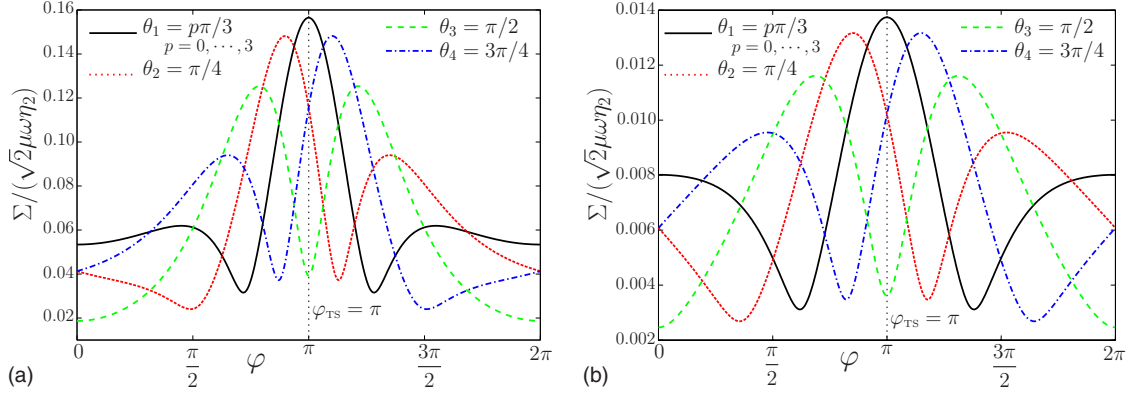
FIG. 6. (Color online) Variations of the normalized time-rms surface stress along the cell wall for RC locations corresponding to $\{\theta_k\}_{k=1,\ldots,5}$, $\rho = 5R_0$ for (a) and $\rho = 10R_0$ for (b).

C. Direct guiding

In terms of Dd aggregation through direct guiding, the direction of TC relative to the RC is clearly of primary importance. In the following, we focus our attention on this directional guiding of a RC mediated by the signal transmitted by the TC. Considering the mechanotransduced signal at the RC's surface, one can express the stress at any point M locally positioned by φ on the cell surface (see Fig. 5) by expanding Eqs. (31) in which Z is taken as

$$Z_\varphi = \frac{z_M - a_0}{R_0 e^{i\theta_0}} = \frac{\rho}{R_0} e^{i(\theta - \theta_0)} \left(1 + \frac{R_0}{\rho} e^{i\varphi} \right). \tag{33}$$

As noted in Sec. II B, the mechanotactic signal is instantly transmitted from the TC to the RC's surface. However, the effectiveness of mechanotransducers at the cell's surface is subject to a certain level of latency. In addition, the internal process of signal integration often leads to a time averaging of the mechanotactic signal [13]. Hence, the behavioral response of the RC is based on the available signal directly connected to the surface stress. The variations in time of the surface stress being sinusoidal and identical for each components, the signal can simply be taken as the time-rms surface stress, denoted $\Sigma(M)$ in the sequel. By definition

$$\Sigma(M) = \langle \| \tilde{\boldsymbol{\sigma}} \cdot \hat{\mathbf{n}} \|^2 \rangle^{1/2} = \langle f_N^2 + f_T^2 \rangle^{1/2}, \tag{34}$$

where $\hat{\mathbf{n}}$ is the local unit outward normal vector and f_N (respectively, f_T) is the normal (respectively, tangential) stress expressed as

$$f_N(M) = \tilde{\sigma}_{xx}(Z_\varphi)\cos^2(\theta + \varphi) + \tilde{\sigma}_{yy}(Z_\varphi)\sin^2(\theta + \varphi)$$
$$+ \tilde{\sigma}_{xy}(Z_\varphi)\sin[2(\theta + \varphi)], \tag{35a}$$

$$f_T(M) = \tilde{\sigma}_{xy}(Z_\varphi)\cos[2(\theta + \varphi)] + \frac{1}{2}[\tilde{\sigma}_{yy}(Z_\varphi) - \tilde{\sigma}_{xx}(Z_\varphi)]\sin[2(\theta$$
$$+ \varphi)] \tag{35b}$$

in terms of the perturbed stress tensor $\tilde{\boldsymbol{\sigma}}$, given by Eqs. (31) and (32), and using the parametrization Z_φ given by Eq. (33). The time rms in Eq. (34) simply leads to a factor $1/\sqrt{2}$ in presence of sinusoidal time variations of the traction, and in

addition all the components of $\tilde{\boldsymbol{\sigma}}$ are in phase as can be seen from Eqs. (31).

The values of $\Sigma(\varphi)$, for $0 \leq \varphi < 2\pi$, represent the complete mechanotactic signal transmitted by the TC and available to the RC, which is deprived of sense of orientation. To be directly guided toward the TC and initiate an approach phase, a RC must find a unique way to determine the transmitted signal direction, denoted as φ_{TS}, based on $\Sigma(\varphi)$. By the definition of the local coordinate system in Fig. 5, $\varphi_{TS} = \pi$ is the true answer. From a navigation standpoint, this direction that the RC needs to be going is called the bearing and is measured with respect to a fixed frame of reference (defined here by the conformal x axis and its directly normal axis, the y axis). Hence, for each RC placed in the stimulus field, the bearing is given by $\alpha_b = \theta + \varphi_{TS} = \theta + \pi$.

It is shown in the sequel that the detection by the cell of the maximum value of $\Sigma(\varphi)$ provides a unique input to the elementary control system of the cell to decide the direction it should be going. This unique input can be considered to be the angle denoted as φ_{max} for which $\Sigma(\varphi_{max})$ is maximum. Note that when the RC moves, its exposition to the stimulus field changes and therefore φ_{max} also changes, which mathematically means that φ_{max} is a function of (ρ, θ). Again from the navigation standpoint, φ_{max} defines the direction that the cell is actually going which is called the heading and is measured by $\alpha_h = \theta + \varphi_{max}$ in the chosen frame of reference. To understand the influence of RC's position (ρ, θ) in detecting the transmitted signal direction φ_{TS}, we display two related results: the variations of the signal Σ with φ for different values of ρ and θ in the stimulus field, and the map of the values of the relative difference between φ_{max} and φ_{TS} in the surroundings of the TC.

Figure 6 shows the variations of the mechanical stress at the surface of several RCs, which confirm the possibility of direct guiding based on the resolution of φ_{max}. For RCs located along the lines $\theta_1 = 0$, $\pi/3$, $2\pi/3$, and π, we have exactly $\varphi_{max} = \varphi_{TS}$. These values of θ_1 refer to the directions of extension or retraction of the cell wall (see Fig. 4) due to the pulsatile variations of $\eta_2(t)$. For RCs not aligned along the lines of pseudopod extension or retraction of TC's wall, φ_{max} is shifted with respect to φ_{TS}. The maximum relative shift is 25% (respectively, 14%) at a distance $\rho = 10R_0$ (respectively, $\rho = 5R_0$) for the value $\theta_3 = \pi/2$. It is obtained
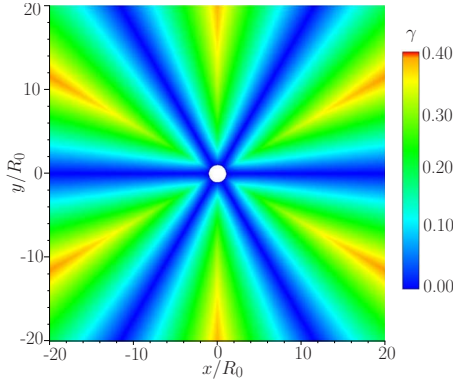
FIG. 7. (Color online) Map of the relative angular dispersion, $\gamma = |\varphi_{max}/\varphi_{TS} - 1|$, in the stimulus field in a square domain $[-20, 20]^2$ around the TC. The circular region, of unit radius and centered at the TC, has been excluded as the stimulus field is undefined at the origin.

when the RC is equally subject to two pseudopods in the directions $\varphi = \pi/3$ and $\varphi = 2\pi/3$. However, for mechanosensing cells situated slightly away from these "symmetry lines," the situation is much less critical. Indeed, cells along the lines $\theta_2 = \pi/4$ and $\theta_3 = 3\pi/4$ can sense a maximum stress that is shifted by only 14% (respectively, 8%) at a distance $\rho = 10R_0$ (respectively, $\rho = 5R_0$). Comparing Figs. 6(a) and 6(b), one notices that the relative angular dispersion, $\gamma = |\varphi_{max}/\varphi_{TS} - 1|$, of the signal maxima decreases with the distance ρ to the TC. Thus, despite this angular dispersion in the signal, cells can still be directly guided by the mechanotactic stimulus, which appears more "focused" as the RC moves toward its goal. As expected, the intensity of the absolute maxima increases when ρ decreases, i.e., when the RC gets closer to the TC.

The analysis above is elucidated by considering the map of the relative angular dispersion, $\gamma = |\varphi_{max}/\varphi_{TS} - 1|$, in the stimulus field. This map is shown in Fig. 7 together with one-dimensional variations of γ along circular arcs in Fig. 8(a) and converging ray lines in Fig. 8(b). These graphs confirm the earlier conclusions based on the variations of the normalized time-rms surface stress. The symmetric feature of the map of γ is directly connected to the symmetry of the pseudopods in the idealized cell boundary evolution considered herein (see Sec. IV C and Fig. 4). With the given color (respectively, grayscale) code for the flooded contour levels, one can clearly see in blue (respectively, dark gray) the regions where the angular dispersion is minimal (below 10%). It is likely that the direct guiding of the RC toward the TC is ineffective in these regions, which are centered around the directions of extension or retraction of the pseudopods corresponding to $\theta_k = k\pi/3$, with $k = 0, \ldots, 5$. On the contrary, in regions centered in between the directions of the pseudopods, i.e., $\theta_{k'} = k'\pi/3 + \pi/6$, with $k' = 0, \ldots, 5$, the angular dispersion is maximal and continuously decreases as the RC gets closer to the TC, which relates to the focusing of the mechanotactic signal mentioned above. In summary, the map of the relative angular dispersion (together with its one-dimensional counterparts in Fig. 8) reveals the relatively high directivity of the mechanotactic signaling, especially
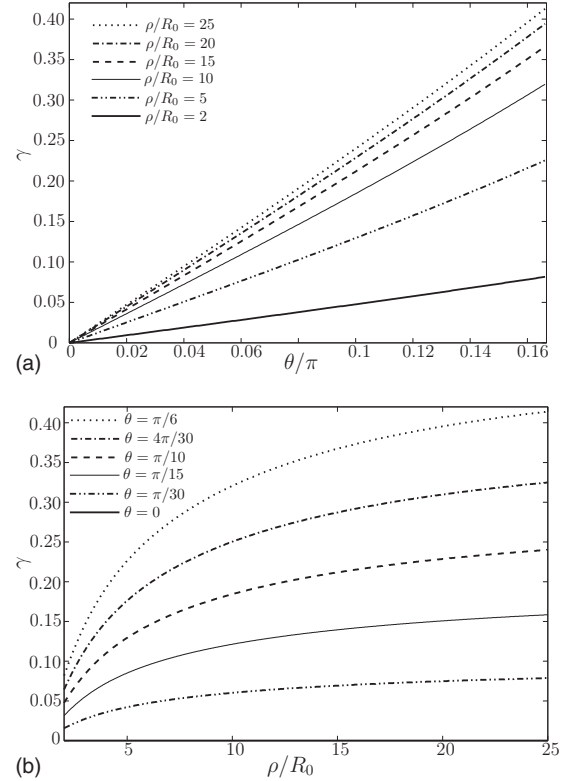

FIG. 8. Variations of the relative angular dispersion, $\gamma = |\varphi_{max}/\varphi_{TS} - 1|$: (a) along circular arcs centered about the TC with varying radii ρ/R_0; (b) along ray lines converging toward the TC and corresponding to varying orientations θ.

when compared to the concurrent chemotactic signaling whose potential directivity is intrinsically limited by the diffusive nature of its communication channel.

The above analysis is an investigation of the dependence of the mechanotactic signaling with distance and direction. It sheds light on this not well-documented signaling process for the direct guiding of amoeboid cells. However, this analysis does not allow one to conclude on the possible and complete direct guiding of any RC cell placed in the stimulus field. For that, a dynamic model of the stimuli-controlled locomotion, accounting for the ubiquitous presence of noise, is required. Such a model is introduced and discussed in the next section.

VI. MODEL FOR THE STIMULI-CONTROLLED CELL MOVEMENT

A. Description of the model

We now consider the next level of complexity in modeling the initial stages of Dd aggregation—the movement of the cells (RCs) in response to the mechanotactic stimulus field generated by a TC as described in Sec. IV and further discussed in Sec. V. To model stimuli-controlled locomotion, we make the central assumption that the cell uses its mechanodetecting capability as a sense of orientation. In other words, the cell keeps moving in the local and varying direction given by the maximum of surface stress, i.e., given by φ_{max}, as considered in the direct guiding in Sec. V C. Exactly

how cells accomplish this through their internal control system is unspecified; only the end result is modeled.

The question is to know whether a RC placed anywhere in the stimulus field can actually reach its goal, i.e., the TC, through a direct guiding motion based on the above model rule. The continuous track path of any RC subject to the above model is represented by small straight-line steps of size ϖ in the direction of the heading $\alpha_h = \theta + \varphi_{max}$ presented in Sec. V C. To best represent the real continuous movement of an actual Dd cell, the step size must be small enough compared to the cell's characteristic length, i.e., $\varpi \ll R_0$. By enforcing such a requirement, the outcome of that modeling approach yields results independent of the step size.

The model devised here would not be realistic without accounting for the ubiquitous presence of noise which may have disruptive behavioral effects. This so-called behavioral noise can be divided into two broad categories: the stimulus noise and the response noise [4]. The stimulus noise, also known as intensity noise, may have different origins such as channel noise, environmental or background noise, and receptor noise. In the present framework, the channel, environmental, and receptor noises are indistinguishable. In order to account for the global effects of stimulus noise together with external perturbing factors (such as the possible presence of other cells in the neighborhood of the RC), a fixed level of background noise is considered throughout the stimulus field. In addition, the response noise may have different origins such as motor noise and developmental noise which cannot be appropriately included within the present idealized modeling framework. In the sequel, the response noise is therefore discarded and the stimulus noise may simply be referred to as noise without any possible confusion.

Noise can generally be assumed to be random fluctuations with a normal distribution [50]. In the sequel, the background noise is considered to have a normal distribution fully characterized by its noise level, denoted NL and defined as the ratio of the amplitude of noise to the amplitude of the signal. The noise level can simply be expressed in terms of the signal-to-noise ratio (SNR), NL=SNR$^{-1/2}$. To our knowledge, there is no report in the literature of the actual magnitude of NL. However, and as discussed above, there are numerous potential sources for mechanical noise which has to be accounted for. The objective in the present work is to prove that despite the presence of possibly high NL noise, mechanotactic guiding remains effective.

B. Effects of the stimulus noise

Adding a given level NL of isotropic stimulus noise affects the signal $\Sigma(\varphi)$ and hence reduces the capability of any RC to seek the best estimate for φ_{TS}. Consequently, the direction φ_{max} detected and selected by the cell as its direction of locomotion is affected. It is informative to visualize these effects on maps of the relative angular dispersion, $\gamma = |\varphi_{max}/\varphi_{TS} - 1|$, in the stimulus field. Three noise levels, NL=10%, 25% and 50%, are considered and the maps of γ are shown in Figs. 9(a)–9(c) respectively. These maps are to be compared to the reference map without noise presented in Fig. 7.
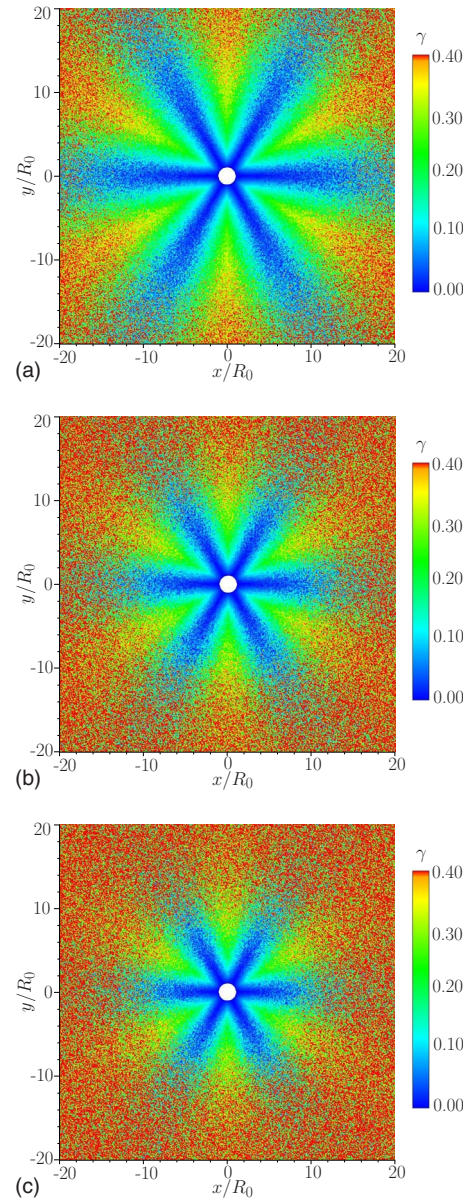

FIG. 9. (Color online) Map of the relative angular dispersion, $\gamma = |\varphi_{max}/\varphi_{TS} - 1|$ affected by stimulus noise. The circular region, of unit radius and centered at the TC, has been excluded as the stimulus field is undefined at the origin. Three noise levels are considered: (a) NL=10%; (b) NL=25%; (c) NL=50%.

As expected, the isotropic stimulus noise has an increasing effect with the distance ρ to the TC, irrespective of the NL of the maps in Fig. 9. From a modeling standpoint, the effects of the stimulus noise readily improve the representation of the real environment by the model for the initial Dd aggregation. Indeed, when considering the map of γ without noise (Fig. 7), it has been noted that the angular dispersion for cells placed very close to the directions θ_k of pseudopod extensions or retractions is extremely low, so that one can expect an almost perfect direct-guiding by the mechanotactic signal even at very large distance ρ from the TC. This fact is better appreciated in Fig. 8(b) for $\theta = 0$ and $\theta = \pi/30$. In both of these cases, the angular dispersion reaches a plateau of low magnitude for large values of ρ, suggesting an almost
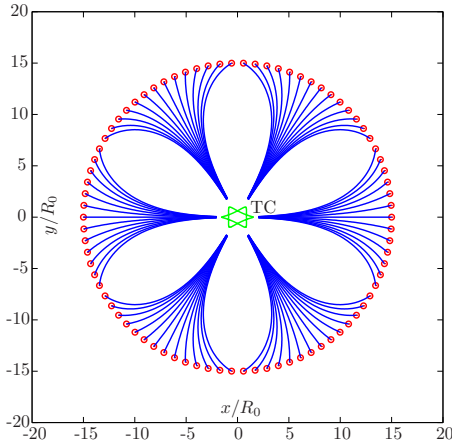
FIG. 10. (Color online) Track paths of the centers of 82 RCs initially distributed evenly along a circle of radius $\rho_0 = 15R_0$ and centered about the TC, which is schematically shown. The initial positions of the centers of the RCs are given by the circles; NL=0 and $\varpi/R_0 = 0.01$.

unbounded detection range of the TC by the RC. In the presence of noise, one clearly notices in Fig. 9 that the detection range is limited for all directions of motion; more precisely, the lower the NL, the longer the detection range.

C. Track paths

In this section, we report the results of an implementation of the model presented and characterized in Sec. VI A to determine the track paths of collections of RCs placed at different locations in the stimulus field. Note that even when a collection of RCs is considered, we continue to use the isolated subsystem assumption of Sec. II A. Each individual direct-guided motion of a RC is considered only in the presence of the TC and without any other RCs, and the independent motions for all RCs in the collection are then superimposed. We add that the tracking of the paths followed by the RCs consist in tracking the paths of their respective conformal centers, i.e., the centers of the cells, as the RCs are assumed to have a circular shape (Sec. V A).

First we consider two collections of RCs directly guided in the absence of noise. The first collection is made of RCs evenly distributed along a circle centered about the TC. The corresponding track paths are represented in Fig. 10 and provide a very symmetric six-lobe pattern directly correlated with the six pseudopod extensions or retractions producing the mechanotactic signal. These track paths confirm the assumptions given in Sec. V C and based on the map of relative angular dispersion: cells initially placed very close to the pseudopod lines $\theta_k = k\pi/3$, with $k = 0, \ldots, 5$, are subject to an almost straight-line direct guiding toward the RC. On the other hand, RCs initially located in between the pseudopod lines, close to the lines $\theta_{k'} = k'\pi/3 + \pi/6$, with $k' = 0, \ldots, 5$, are subject to less direct guiding, which is not surprising given the high angular dispersion found there. However, these results confirm the possibility of a direct guiding even for the cells placed in these critical regions of maximal γ. In the absence of noise, the same pattern as the one in Fig. 10 is
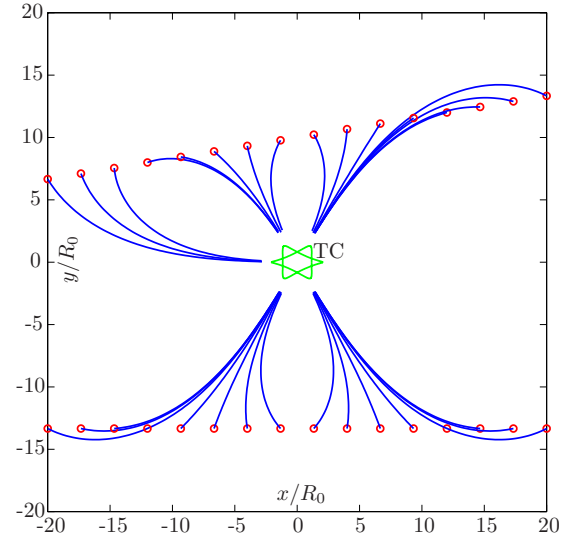

FIG. 11. (Color online) Track paths of the centers of 32 RCs initially distributed evenly along a two straight lines. The TC is schematically shown and the initial positions of the centers of the RCs are given by the circles; NL=0 and $\varpi/R_0 = 0.01$.

observed when changing the value of the radius of the circle on which the RCs are distributed. This leads to the strong conclusion that, in the absence of noise, any cell placed in the stimulus field (even at very large distances ρ from the TC) can be directly guided by the mechanotactic signal.

As a further illustration, we consider a second collection of RCs evenly distributed along two straight-line segments. The associated track paths are given in Fig. 11 and are easily explained by extending the same conclusions as for the circular distribution apply in that case.

Having considered these two ideal cases in the absence of stimulus noise, we now turn to the noisy direct guiding of the same collection of RCs evenly distributed along a circle. The corresponding track paths for three different noise levels, NL=10%, NL=25%, and NL=50%, are shown in Figs. 12(a)–12(c) respectively.

As expected, when the level of noise is increased, the track paths become less and less straight and direct, even for the cells located near an axis of pseudopod extension or retraction θ_k. This is in agreement with the analysis of the maps of relative angular dispersion in the presence of noise, shown in Fig. 9. At large distances from the TC, when the RCs are initially released, this behavior is more apparent and for large noise levels very closely resemble a two-dimensional random walk [see Fig. 12(c)]. This resemblance to the patterns of 2D random walks is readily explained by the fact that the effects of noise overcome those of the mechanotactic signaling. Indeed, at distances $\rho \simeq \rho_0 = 15R_0$, the amplitude of the mechanotactic signal is much lower than the amplitude of noise which precludes effective direct guiding. The guiding therefore is indirect until the RC finally reaches a region of the stimulus field much closer to the TC where direct guiding is recovered because of the increased amplitude of the mechanotactic signal and the track paths become less tortuous. The leading effects of direct guiding are clearly visible for all noise levels in a circular region
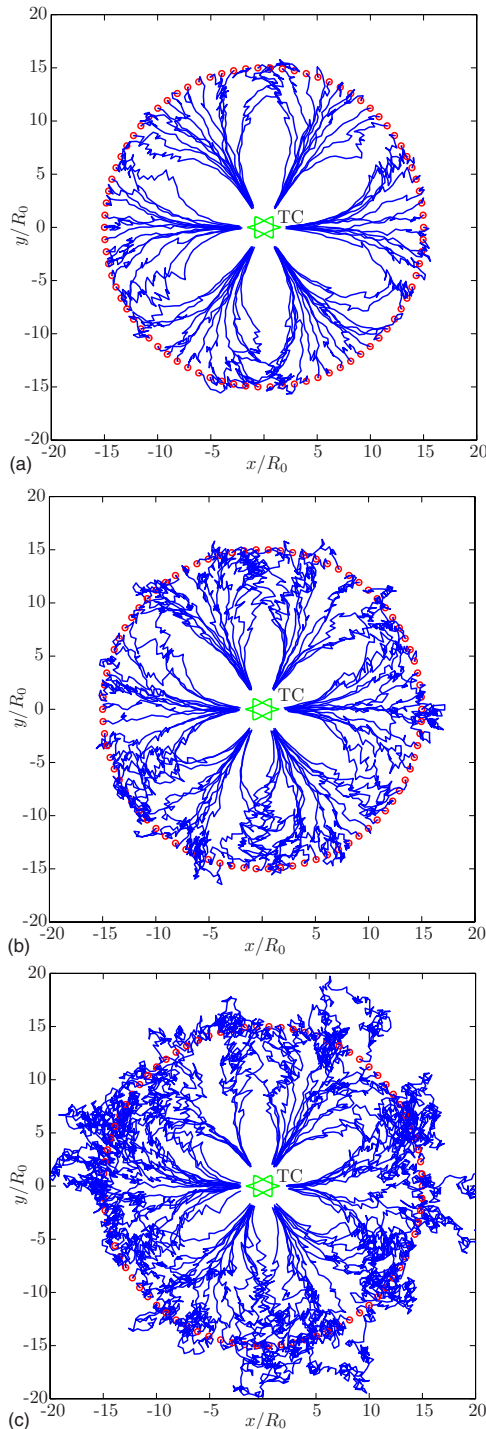
FIG. 12. (Color online) Track paths of the centers of 82 RCs initially distributed evenly along a circle of radius $\rho_0 = 15R_0$ and centered about the TC, which is schematically shown. The initial positions of the centers of the RCs are given by the circles; $\varpi/R_0 = 0.05$ and (a) NL=10%, (b) NL=25%, and (c) NL=50%.

centered about the TC. The extent of this region, the direct-guiding region (DGR), is fully determined by the noise level.

In summary, in the presence of noise, the direct guiding is still effective but only in the DGR centered around the TC, the dimensions of which are controlled by the noise level. Outside the DGR, the movement of the RCs is indirectly
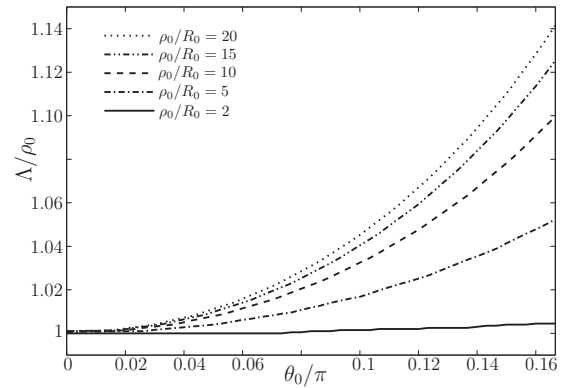

FIG. 13. Evolution of the relative path length as a function of the initial angular position θ_0 of the RC. Five initial distances ρ_0 to the TC are considered.

guided leading to patterns characteristics of random walks.

D. Path length

A more quantitative analysis of the track paths is possible by considering a simple metric for these paths based on the path length denoted as Λ. To facilitate comparisons, the relative path length Λ/ρ_0 is considered, where ρ_0 corresponds to the initial distance between the RC and the TC. The variations of Λ/ρ_0 as a function of the initial angular position θ_0 (in the interval $0 \le \theta_0 \le \pi/6$ given the symmetries of the system) are shown in Fig. 13 in the absence of noise. As expected from the analysis of Fig. 10, the path length is minimal and equal to the initial distance ρ_0 to the TC when the RC is perfectly aligned with the pseudopod extension or retraction at $\theta_0 = 0$. Conversely, the relative path length is maximal when the RC is initially aligned in between two pseudopod extensions or retractions, here for $\theta_0 = \pi/6$. Moreover, for RCs initially aligned along the line $\theta_0 = \pi/6$, Λ/ρ_0 rapidly increases with the distance ρ_0 to the TC. For RCs initially located at a distance $\rho_0 = 20R_0$ from the TC, there is an almost 15% difference between the path lengths of two RCs initially along the lines $\theta_0 = 0$ and $\theta_0 = \pi/6$.

In the presence of a noise level of 10%, the above results are significantly modified as can be seen in Fig. 14. For initial distances $\rho_0 \le 7.5R_0$, the relative path length is only slightly affected. For larger distances, the path lengths are increased for all values of θ_0 and for values $\rho_0 \ge 12.5R_0$, the path lengths no longer exhibit an increasing trend with respect to θ_0. Instead, the path lengths fluctuate around a mean value practically constant in the interval $0 \le \theta_0 \le \pi/6$. From these observations, one can indirectly conclude that the radius of the DGR, ρ_{DGR}, is close to $7.5R_0$ with NL=10%. The same study for NL=25% (respectively, NL=50%) provides $\rho_{DGR} \simeq 5R_0$ (respectively, $\rho_{DGR} \simeq 3R_0$).

E. Eulerian pattern of initial aggregation

The study of the Lagrangian tracking of RCs in the stimulus field of the TC presented in Secs. VI C and VI D suggests the possibility of observing mesoscopic-scale patterns, formed by surrounding RCs, characterized by the signaling
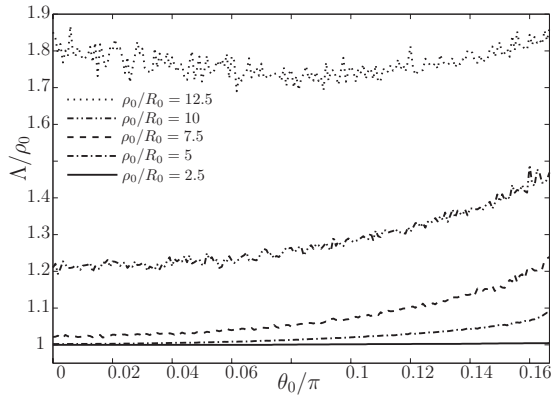
FIG. 14. Evolution of the relative path length as a function of the initial angular position θ_0 of the RC. Five initial distances ρ_0 to the TC are considered, with NL=10%.

motion of a microscopic TC—in this present case, the six lobe patterns centered about the directions of extensions or retractions of the TC. We obtain the pattern formed by large numbers of surrounding RCs moving under the influence of the mechanotactic signaling of a TC by computing the probability density function (PDF) of passage of a RC in the stimulus field. Note that such an approach is more in line with the Eulerian approach considered by experimentalists. For the present results, the PDF is computed by randomly releasing 16 million RCs in a given region of the stimulus field and by tracking the cell positions as in Sec. VI C. Each cell position is then mapped onto a 2D refined regular grid comprising 500^2 points. By properly normalizing the number of passages at each grid point, one obtains the Eulerian map of the PDF of passage of a stimuli-controlled RC, which is shown in Fig. 15 in the absence of noise.

This map of the PDF of passage confirms the expectations based on the Lagrangian tracking of RCs. A clear symmetric six-lobe mesoscopic pattern is visible in Fig. 15. While the
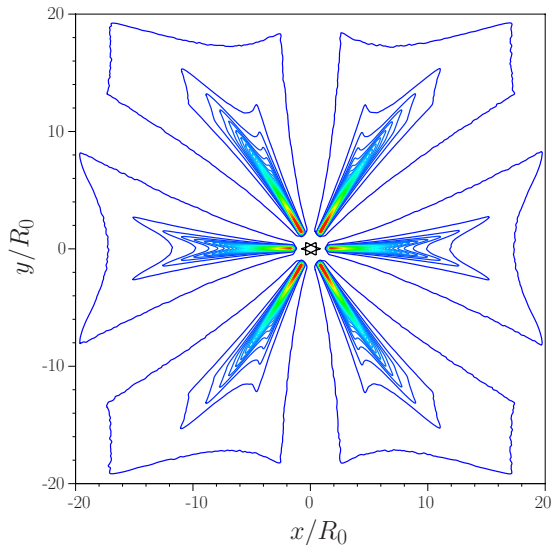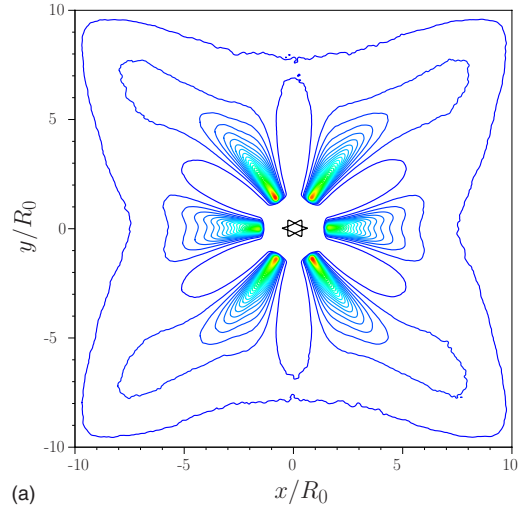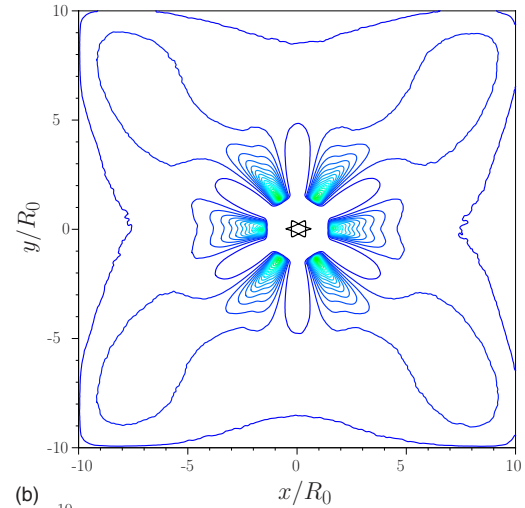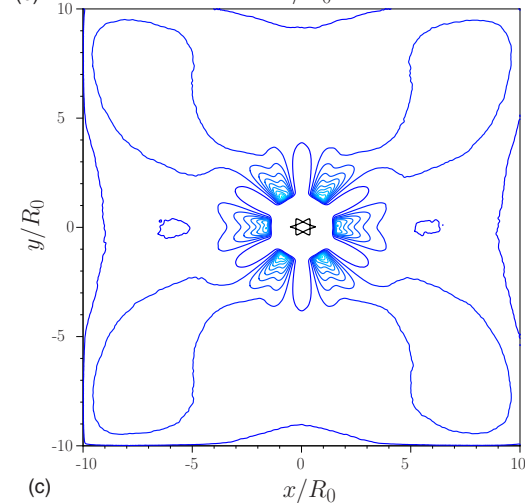

FIG. 15. (Color online) Contours of the PDF of passage of a RC in its guided motion within the stimulus field. The plot comprises 50 equally distributed contours between 10^{-6} and 2.510^{-4}, with $\varpi/R_0=0.05$.

(a)

(b)

(c)

FIG. 16. (Color online) Contours of the PDF of passage of a RC in its guided motion within the stimulus field. The plot comprises 40 equally distributed contours between 2.10^{-6} and 10^{-4}; $\varpi/R_0=0.05$ and (a) NL=10%, (b) NL=25%, and (c) NL=50%.

specific symmetric feature of this Eulerian map is artificial in that it is a result of a specific imposed evolution of the TC's cell surface, it is important to observe how the pseudopod extension or retraction of the TC leads to a clear and intense

mesoscopic lobe features in the PDF of passage. The existence of such lobes is another revealing feature of the high directivity of the mechanotactic signaling, especially when compared to chemotaxis. Indeed chemotactic signaling cannot be directive due to its diffusive nature which tends to homogenize the density of chemical released to generate the signal. In this case, experimental mesoscopic observation of such a lobe of the PDF of passage would suggest microscopic TC pseudopod extension or retraction motions. It also provides strong evidence for the existence of direct guiding through mechanotactic signaling and possibly the quantification of the stimulus noise in the system.

The presence of noise affects the map of the PDF of passage in the stimulus field as can be shown in Fig. 16 for three different noise levels. The main effect induced by the presence of noise is to reduce the extent of the lobes which are now confined to the directly guided region. This observation is in good agreement with the Lagrangian observations in Fig. 12.

We remark that, for the sake of theoretical simplicity and clarity, we have considered somewhat idealized signaling herein, but our formulation and approach are indeed quite general and could be extended to model general cell signaling encountered in nature. More importantly, the salient insights and conclusions we obtain here for this idealized mechanotactic signaling should apply to real-life mechanotactic signaling. We have shown the ability to decipher the microscopic mechanotactic signaling produced by the TC by observing the mesoscopic aggregative behavior of the RCs in its neighborhood. Such lobes have been observed experimentally and reported by Kessin in [51] (Fig. 1) for Dd cells aggregating. A purely chemotactic explanation was proposed by Kessin to explain the existence of these streams of Dd cells. The mechanotactic signaling, however, was not considered in [51]. Despite the limitations of our model, we hypothesize here the possible mechanotactic origin of these streams of Dd experimentally observed.

VII. CONCLUSIONS

The effects of mechanotactic signaling in the initial aggregation of amoeboid cells are investigated. A specific-modeling approach based on known biological evidences is devised to elucidate the hydrodynamic aspects of mechanotaxis at premorphogenesis. This model suggests a signal detection based on the resolution by each cell of the absolute maximum of the mechanical stress at its surface. With this signal detection, it was found that aggregation can indeed be initiated by means of mechanotaxis.

In this framework, we quantify the cell-cell mechanical signaling capabilities. The results we present show that a RC can be directly guided by the TC through mechanotactic signaling. By changing its shape, the TC generates a mechanical signal transmitted through the fluid flow which leads to a specific mechanical stress on any RC's surface located in the stimulus field. The resolution of the maximum of this surface

stress serves as an indicator of the transmitted signal direction. The analysis presented in this paper is based on an idealized evolution of the shape of the cell but the mathematical theory allow for a general treatment of the cell shape.

We show that a RC can detect the signal direction with a limited angular dispersion, which decreases as the source is approached. In real field situations, the mechanotactic signal would be subject to ubiquitous mechanical noise. The effects of background noises of varying levels are studied and reveal that the noise level controls the extent of a directly guided region centered about the TC. Outside that region, the cell's motility is no longer controlled by the mechanotactic signal and hence the cell becomes indirectly guided.

The Lagrangian tracking of the path of RCs placed in the stimulus field is performed and confirms the direct guiding of all cells, including those placed in the regions of high angular dispersion of the mechanotactic signal. According to our model, we can conclude that it is possible to initiate aggregation of amoeboid cells based entirely on mechanotaxis.

The study of the PDF of passage through the stimulus field reveals the presence of a high-intensity mesoscopic lobe associated with each pseudopod extension or retraction of the cell. This specific pattern confirms the high-directivity of mechanotactic signaling and could serve as an experimental mesoscopic indicator of the actual microscopic changes in the cell shape. Given the straightforward generalization of our modeling approach based on a rather idealized cell signaling, the results and conclusions reported here should still hold for complex signaling encountered in nature. It is ultimately hypothesized that the pattern of streams of Dd observed and reported by Kessin in [51] (Fig. 1) might have also a mechanotactic origin.

The present analysis leads to the conclusion that mechanotaxis is a likely tropotactic mechanism of directed guiding [4], possibly concurrent with chemotaxis. The possible synergism or competition between these different mechanisms at different stages of cell organization is not yet understood. The fundamental physical laws governing these two mechanisms are extremely different and hence they can be considered completely independently from one another. For instance, any chemotactic model commonly available in the literature could be incorporated in the present modeling approach to study the joint effect of mechanotaxis and chemotaxis. This model also highlights that mechanotaxis, by its very nature, transmits the mechanical signal instantaneously and potentially with a high directivity. In comparison, chemotaxis is known to be slower in transmitting signals, which are poor directionally given the diffusive nature of the mechanisms involved in it [4].

ACKNOWLEDGMENTS

[1] E. Schrödinger, *What is Life?* (Cambridge University Press, Cambridge, England, 1944).

[2] P. T. Macklem, J. Appl. Physiol. **104**, 1844 (2008).

[3] S. Camazine, J.-L. Deneubourg, N. R. Franks, J. Sneyd, G. Theraulaz, and E. Bonabeau, *Self-Organization in Biological Systems* (Princeton University Press, Princeton, NJ, 2001).

[4] D. B. Dusenbery, *Sensory Ecology* (W. H. Freeman and Co., New York, 1992).

[5] C. L. Manahan, P. A. Iglesias, Y. Long, and P. N. Devreotes, Annu. Rev. Cell Dev. Biol. **20**, 223 (2004).

[6] H. Delanoë-Ayari, S. Iwaya, Y. T. Maeda, J. Inose, C. Rivière, M. Sano, and J. Rieu, Cell Motil. Cytoskeleton **65**, 314 (2008).

[7] P. Friedl, S. Borgmann, and E.-B. Bröcker, J. Leukoc Biol. **70**, 491 (2001).

[8] P. N. Devreotes and S. H. Zigmond, Annu. Rev. Cell Biol. **4**, 649 (1988).

[9] J. Hardin and T. Walston, Curr. Opin. Genet. Dev. **14**, 399 (2004).

[10] D. Dormann and C. J. Weijer, Curr. Opin. Genet. Dev. **16**, 367 (2006).

[11] H. Blaser, M. Reichman-Fried, I. Castanon, K. Dumstrei, F. L. Marlow, K. Kawakami, L. Solnica-Krezel, C. P. Heisenberg, and E. Raz, Dev. Cell **11**, 613 (2006).

[12] J. Dalous, E. Burghardt, A. Müller-Taubenberger, F. Bruckert, G. Gerisch, and B. Bretschneider, Biophys. J. **94**, 1063 (2008).

[13] P. A. Janmey and C. A. McCulloch, Annu. Rev. Biomed. Eng. **9**, 1 (2007).

[14] C. Wilhelm, C. Rivière, and N. Biais, Phys. Rev. E **75**, 041906 (2007).

[15] C. Rivière, S. Marion, N. Guillén, J.-C. Bacri, F. Gazeau, and C. Wilhelm, J. Biomech. **40**, 64 (2007).

[16] E. Décavé, D. Rieu, J. Dalous, S. Fache, Y. Bréchet, B. Fourcade, M. Satre, and F. Bruckert, J. Cell. Sci. **116**, 4331 (2003).

[17] M. F. Coughlin and G. W. Schmid-Schönbein, Biophys. J. **87**, 2035 (2004).

[18] S. Kidoaki and T. Matsuda, J. Biotechnol. **133**, 225 (2008).

[19] M. Singh, C. Berkland, and M. S. Detamore, Tissue Eng. **14**, 341 (2008).

[20] E. Evans, Biophys. J. **64**, 1306 (1993).

[21] R. R. Kay, Curr. Opin. Microbiol. **5**, 575 (2002).

[22] R. H. Kessin, *Dictyostelium: Evolution, Cell Biology, and the Development of Multicellularity* (Cambridge University Press, Cambridge, England, 2001).

[23] J. T. Bonner, *The Social Amoebae: The Biology of Cellular Slime Molds* (Princeton University Press, Princeton, NJ, 2009).

[24] S. J. Annesley and P. R. Fisher, Mol. Cell. Biochem. **329**, 73 (2009).

[25] A. A. Biewener, *Animal Locomotion* (Oxford University Press, New York, 2003), Chap. 6, pp. 151–162.

[26] T. Lämmermann and M. Sixt, Curr. Opin. Cell Biol. **21**, 636 (2009).

[27] A. M. Turing, Philos. Trans. R. Soc. London, Ser. B **237**, 37 (1952).

[28] E. M. Purcell, Am. J. Phys. **45**, 3 (1977).

[29] E. Lauga and T. R. Powers, Rep. Prog. Phys. **72**, 096601 (2009).

[30] A. Shapere and F. Wilczek, J. Fluid Mech. **198**, 557 (1989).

[31] J. E. Avron, O. Gat, and O. Kenneth, Phys. Rev. Lett. **93**, 186001 (2004).

[32] J. Happel and H. Brenner, *Low Reynolds Number Hydrodynamics* (Prentice-Hall, New York, 1965).

[33] L. E. Becker, S. A. Koehler, and H. A. Stone, J. Fluid Mech. **490**, 15 (2003).

[34] Z. Nehari, *Conformal Mapping* (Dover, New York, 1952).

[35] G. Pólya and G. Szegö, *Isoperimetric Inequalities in Mathematical Physics* (Princeton University Press, Princeton, NJ, 1951).

[36] P. L. Duren, *Univalent Functions* (Springer-Verlag, Heidelberg, 1983).

[37] L. V. Ahlfors, *Conformal Invariants* (McGraw-Hill, London, 1973).

[38] M. Tsuji, *Potential Theory in Modern Function Theory* (Maruzen Co. Ltd., Tokyo, 1959).

[39] E. Sharon and D. Mumford, Int. J. Comput. Vis. **70**, 55 (2006).

[40] Y. Fukui, T. Q. P. Uyeda, C. Kitayama, and S. Inoué, Proc. Natl. Acad. Sci. U.S.A. **97**, 10020 (2000).

[41] N. I. Muskhelishvili, *Some Basic Problems of the Mathematical Theory of Elasticity. Fundamental Equations, Plane Theory of Elasticity, Torsion and Bending* (P. Noordhoff Ltd., Gröningen, Holland, 1963).

[42] W. E. Langlois, *Slow Viscous Flow* (The Macmillan Co., New York, 1964).

[43] S. Tanveer and G. L. Vasconcelos, J. Fluid Mech. **301**, 325 (1995).

[44] V. Vogel and M. P. Sheetz, Curr. Opin. Cell Biol. **21**, 38 (2009).

[45] H. C. Berg, *Escherichia coli in Motion* (Springer-Verlag, New York, 2004).

[46] S. Na, O. Collin, F. Chowdhury, B. Tay, M. Ouyang, Y. Wang, and N. Wang, Proc. Natl. Acad. Sci. U.S.A. **105**, 6626 (2008).

[47] S. Kim and S. J. Karrila, *Microhydrodynamics: Principles and Selected Applications* (Dover, New York, 1991).

[48] M. D. Finn and S. M. Cox, J. Eng. Math. **41**, 75 (2001).

[49] S. K. Sen, Z. Angew. Math. Phys. **40**, 139 (1989).

[50] D. B. Dusenbery, *Living at Micro Scale: The Unexpected Physics of Being Small* (Harvard University Press, Cambridge, MA, 2009).

[51] R. H. Kessin, Nature (London) **422**, 481 (2003).